Spectral correlations in a fiber-optical parametric oscillator

Mohamed Touil⬤, Rezki Becheker⬤, Thomas Godin⬤,* and Ammar Hideur⬤

CORIA UMR 6614, CNRS, Université de Rouen Normandie, INSA Rouen, 76800 Saint Etienne du Rouvray, France

Tailoring wavelength correlations in fiber-optical sources through nonlinear phenomena could drive many quantum optics applications. However, to date, such correlations have not been explored within fiber-optical parametric oscillators (FOPO), which are now widespread wavelength-agile sources. We experimentally investigate the real-time dynamics of a synchronously pumped picosecond FOPO with a combination of statistical tools using time-stretch spectroscopy. The study of wavelength correlations allows us to unveil particular spectrotemporal dynamics and correlation patterns. Specifically, we demonstrate that combining mutual information (MI) analysis and least-squares regression with large ensembles of shot-to-shot spectra allows to efficiently track energy transfers from pump to parametric waves. In addition, we show that tuning the FOPO parameters enables the shaping of spectral correlations to a certain extent.

I. INTRODUCTION

The complex dynamics of optical systems has attracted scientists for decades and the emergence of real-time temporal and spectral measurement techniques has recently opened new opportunities by enabling in-depth characterization of ultrafast or nonrepetitive events. In the temporal domain, the development of time lenses has, for instance, allowed the full-field characterization of partially coherent waves [1] or soliton dynamics in mode-locked lasers [2] and provided new insights in their transient dynamics. In the spectral domain, dispersive Fourier transformation (DFT) is a powerful tool for the continuous acquisition of real-time spectra on long timescales [3,4]. It indeed enabled the real-time spectral characterization of ultrafast laser systems, from unveiling their build-up dynamics [5] to probing soliton bound states [6,7]. This ability to record large ensembles of spectra then allows use of statistical metrics to describe the dynamical behaviors of light sources. Higher-order moments and Pearson correlations, for instance, have been used for understanding the complex processes involved in supercontinuum generation [8,9]. Spectral correlation indeed revealed the intrinsic dynamics of particular phenomena in optical systems such as modulation instability, four-wave mixing (FWM), random lasing [10–12], and can also be useful when designing FWM-based amplifiers [13]. In fiber-based sources, it has been demonstrated experimentally that spectral correlations resulting from modulation instability and FWM could be shaped through the control of the dispersion maps of liquid- or gas-filled optical fibers [14–16]. This "on-demand" tailoring of frequency correlations could be a valuable tool for building specific sources in quantum optics applications, such as biphoton, twin beam sources [15], or ultrafast frequency combs [17]. These studies, however, concerned "single-pass"

sources, and an actual shaping of frequency correlations within parametric oscillators has not been reported yet and may prove relevant due to the wavelength flexibility of such systems.

In this paper we thereby characterize the dynamics of a fiber-optical parametric oscillator (FOPO) using DFT in order to identify the experimental parameters driving its spectrotemporal properties and correlations. On the one hand, spectrotemporal dynamics and pulse-to-pulse instabilities have recently been studied in bulk $\chi^{(2)}$-based OPOs, which are well-known sources of highly quantum-correlated beams [18], demonstrating that chirp rate, pump power, and cavity detuning, among other parameters, strongly influence the output dynamics [19,20]. For instance, particular dynamics have then been recorded with chaotic or periodic spectrotemporal evolutions. In such $\chi^{(2)}$-based singly resonant cavities, it has also been shown numerically that an extremely rich variety of self-organized structures can be found [21]. On the other hand, FOPOs based on degenerate four-wave mixing (DFWM) have reached enough maturity for many applications, particularly in coherent anti-Stokes Raman scattering microscopy [22,23], due to their broad tuning range, their ability to generate synchronized pulses with widely spaced frequency bands, and their favorable noise properties [24]. A recent study described the build-up dynamics of a FOPO using DFT [25], but wavelengths correlations and the parameters governing their shape have never been investigated to date. Here we then aim at unveiling the spectrotemporal dynamics and particular spectral correlations in a synchronously pumped FOPO using an original combination of different statistical tools including mutual information analysis. Our study is structured as follows. We first present our experimental setup for recording the FOPO dynamics and the combination of statistical tools used to exploit the large ensembles of data. We then use these tools to highlight specific correlation patterns and also to evidence the influence of pump intensity fluctuations on the output dynamics. In this frame,
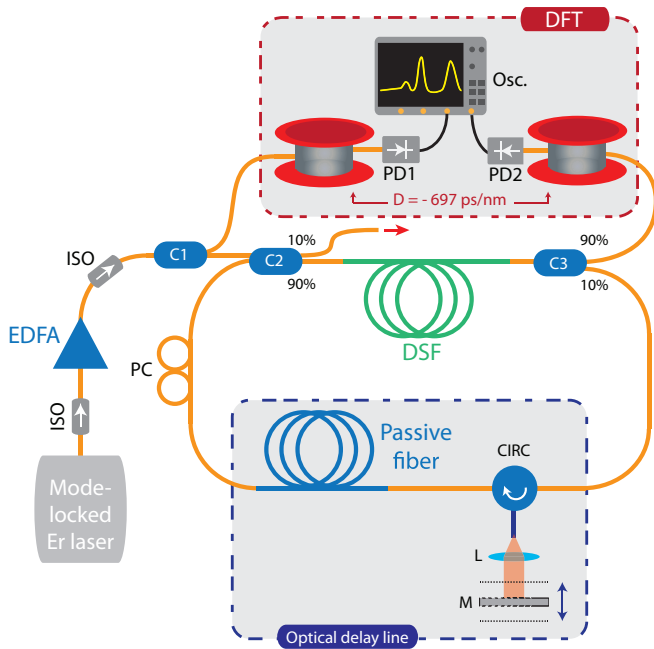
*thomas.godin@coria.fr

FIG. 1. Experimental setup. EDFA: erbium-doped fiber amplifier; ISO: isolator; C: coupler; DSF: dispersion-shifted fiber; CIRC: optical circulator; PC: polarization controller; PD: photodiode; L: lens; M: mirror.
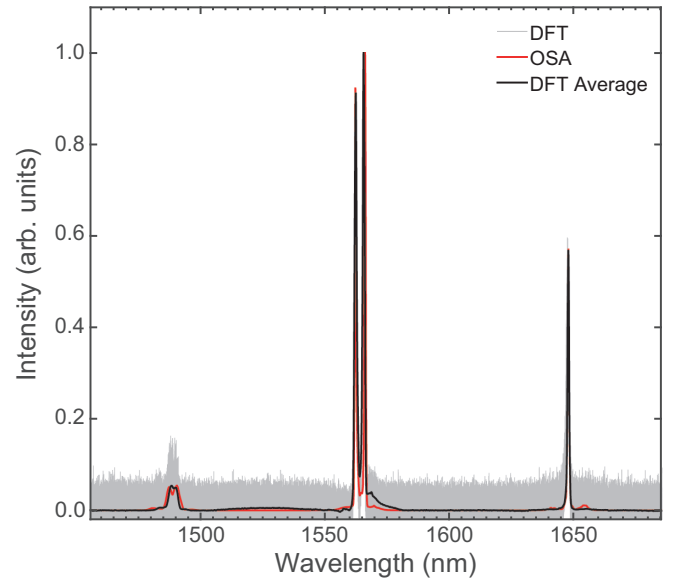

FIG. 2. Real-time spectra recorded using DFT (gray), their average spectrum (black), and comparison with an OSA measurement (red).

we will compare standard Pearson correlation and mutual information (MI) analysis [12,26] for revealing the system dynamics. In addition, we will investigate the spectrotemporal booting dynamics of the system and its convergence toward a steady state. Finally, we will highlight the specific influence of the cavity detuning on the correlation patterns, but more importantly, we will demonstrate how the combination of simple statistical tools can be used to extract insightful data from large ensembles of shot-to-shot spectra. Some perspectives to this work are eventually presented in the frame of the full engineering of spectral correlations in fiber OPOs.

II. EXPERIMENTAL SETUP

Our experimental setup, shown in Fig. 1, is derived from the one developed in Ref. [27] for efficient parametric oscillations around 1.7 μm. A homemade, passively mode-locked erbium-doped fiber laser is used as a pump source and can deliver dissipative solitons with several nanojoules of energy at a repetition rate of 6.1 MHz [28]. Its output wavelength can be tuned from 1549 to 1566 nm using an intracavity diffraction grating. To ensure high stability on long terms, the mode-locked oscillator is operated at low average power of 4.5 mW and generates chirped pulses with 28-ps duration and 2.3-nm average spectral width. The spectrum of the generated pulses exhibits an M shape. This profile is found to be crucial for highlighting the influence of the spectral shape on the FOPO dynamics. The laser pulses are subsequently amplified up to 50 mW of average power using an erbium-doped fiber amplifier (EDFA). The FOPO cavity then consists of 7.7 m of a 4-μm-core dispersion shifted fiber (DSF) acting as the

gain medium for efficient DFWM, 5.4 m of HI1060 fiber, and 8.5 m of UHNA4 fiber for pulse synchronization and operation in the normal dispersion regime in order to overcome the nanojoule energy barrier at around 1700 nm [27]. The FOPO's averaged-zero dispersion wavelength is estimated to be around 1.73 μm. The free-space section of the optical delay line (ODL) is used for fine adjustments of the synchronization of the oscillating pulses with fresh pump pulses. It then allows to synchronization of the pump pulses, either with the resonating signal or idler. In this configuration, the phase-matched signal and idler can be tuned from 1340 to 1513 nm and 1617 to 1876 nm, respectively.

Real-time spectra are recorded at the FOPO's input and output using dispersive Fourier transformation, where time-stretching is obtained using spools of telecommunication-grade fibers with a dispersion of −697 ps nm^{-1} at 1550 nm. The output port of coupler C2 is used for monitoring the pump pulse duration via an autocorrelator, while the pump and FOPO spectra are respectively acquired in the time domain at the 10% port of coupler C1 and the 90% port of coupler C3 using two high-speed 25-GHz photodiodes (New Focus, Inc.) and a real-time 33-GHz oscilloscope (Keysight, Inc.). Taking into account the limited bandwidth of the photodetector and more importantly, the magnitude of the time-stretching process, our system has a spectral resolution of 0.04 nm. The reliability of DFT measurements is ensured by comparing consecutive real-time spectra with standard measurements based on an optical spectrum analyzer (OSA, Anritsu), as shown in Fig. 2, where we achieve a satisfying matching of the spectral components over the full emission range of the FOPO. Note that in the following all the spectra are normalized to the pump intensity. In the next section we detail how specific statistical tools can be used to extract relevant information from shot-to-shot spectra acquired using this setup.

III. STATISTICAL TOOLS

Real-time measurement of shot-to-shot spectra enables the extraction of statistical matrices providing insights on the physical processes based on large sets of experimental data. Wavelength intensity correlations are, for instance, very useful to reveal energy transfers or dependency between different spectral components [8]. On the one hand, correlation is a measure of the linear dependency between two random variables and provides information about the strength and nature—either positive or negative—of this linear relationship. On the other hand, mutual information (MI) analysis is a similar statistical tool quantifying the general dependency between two random variables but might provide a better physical insight as it is a quantitative expression of the information obtained on one variable throughout the observation of another [29]. It then provides a measure of the dependency—linear or nonlinear—between two random variables. MI is for now underused in nonlinear optics but has recently been proved insightful in the study of spectral dynamics in fiber laser systems [12,30]. We then aim here at generalizing its use and evaluating its relevance when studying correlations in nonlinear optical systems. In a discrete domain, the mutual information between variables X and Y is defined as

$$\sum_{y \in Y} \sum_{x \in X} P_{XY}(x, y) \log \left(\frac{P_{XY}(x, y)}{P_X(x) P_Y(y)} \right), \qquad (1)$$

where $P_{XY}(x, y)$, $P_X(x)$, and $P_Y(y)$ are the joint probability mass function and marginal probability mass functions of X and Y, respectively. The estimation of these probabilistic functions from a limited statistical base is a well-known problem in statistics [31]. Among the available solutions, we use histogram estimation, as it is the simplest with the least computational load.

On the one hand, MI dependency maps would then share the same patterns with standard Pearson wavelength correlation maps (as in Refs. [8–11]), yet MI maps are more versatile, as they can visually capture the significance of larger changes due to the log function. On the other hand, MI maps can only have positive values and then do not provide any information regarding the sign of the dependency between the variables. In order to compensate for this drawback, we propose here to combine MI with the standard least-squares (LSQ) method to determine the derivative of the best linear fit between the two random variables in the spectral regions with considerable mutual information. The sign of this derivative indeed identifies the nature of the dependency, either positive or negative. Another reason for using linear regression is imposed by our specific system: the DFWM process corresponds to the annihilation of two pump photons while simultaneously generating idler and signal photons, making the generated photons pair correlated in the quantum sense. The conversion efficiency of this process relates to the number of converted pump photons with respect to the total number of pump photons available at a given wavelength and thereby to the probability of generation of a signal/idler photons pair in spontaneous emission. The joint spectral density function of this probability is approximated by the product of the phase matching and the energy

conservation functions [14,16]. The phase matching of the DFWM process in an optical fiber directly depends on the pump power and wavelength. Consequently, for a specific pump wavelength λ_p, the conversion efficiency only depends on the pump power, and any change in it would induce a change in the FWM gain and subsequently in the conversion efficiency [32]. If λ_{p_0}, λ_{s_0}, and λ_{i_0} are the central wavelengths for pump, signal, and idler, respectively, and Λ_{p_0}, Λ_{s_0}, and Λ_{i_0} their respective spectral widths, let us consider the following variables: $\lambda_p \in [\lambda_{p_0} - \Lambda_{p_0}/2, \lambda_{p_0} + \Lambda_{p_0}/2]$ spanning the pump wavelengths, $\lambda_s \in [\lambda_{s_0} - \Lambda_{s_0}/2, \lambda_{s_0} + \Lambda_{s_0}/2]$ spanning the signal wavelengths, and $\lambda_i \in [\lambda_{i_0} - \Lambda_{i_0}/2, \lambda_{i_0} + \Lambda_{i_0}/2]$ spanning the idler wavelengths. For DFWM with chirped pump pulses, every component within the pump spectrum contributes to the idler (and signal) at a specific wavelength, with a certain proportion dictated by the phase mismatch, and can be written as follows:

$$I(\lambda_i, n) = \int_{\lambda_{p_0} - \Lambda_{p_0}/2}^{\lambda_{p_0} + \Lambda_{p_0}/2} a(\lambda_p, \lambda_i, n) I(\lambda_p, n) d\lambda_p \qquad (2)$$

$$= \int_{\lambda_{p_0} - \Lambda_{p_0}/2}^{\lambda_{p_0} + \Lambda_{p_0}/2} I(\lambda_i, \lambda_p, n) d\lambda_p, \qquad (3)$$

where $I(\lambda_i, n)$ and $I(\lambda_p, n)$ are the idler and pump spectral intensities, and $n \in \mathbb{Z}^{(+)}$ is the pulse number. $a(\lambda_p, \lambda_i, n)$ is the pump-to-idler conversion efficiency for pulse n and $I(\lambda_i, \lambda_p, n)$ is the contribution of pump at λ_p to idler at λ_i for pulse n. In a discrete environment, it then is written

$$I(\lambda_i, n) = \sum_{\lambda_p = \lambda_{p_0} - \Lambda_{p_0}/2}^{\lambda_{p_0} + \Lambda_{p_0}/2} a(\lambda_p, \lambda_i, n) I(\lambda_p, n) \qquad (4)$$

$$= \sum_{\lambda_p = \lambda_{p_0} - \Lambda_{p_0}/2}^{\lambda_{p_0} + \Lambda_{p_0}/2} I(\lambda_i, \lambda_p, n). \qquad (5)$$

For pulse $n + 1$, the spectral intensity at wavelength λ_p changes to $I(\lambda_p, n + 1)$. This intensity fluctuation is denoted $\Delta I_{\lambda_p} = I(\lambda_p, n + 1) - I(\lambda_p, n)$. The change in the idler due to the change of the pump is written as

$$\Delta I_{\lambda_i} = I(\lambda_i, \lambda_p, n + 1) - I(\lambda_i, \lambda_p, n). \qquad (6)$$

The pump intensity fluctuation affects the phase mismatch and thereby modifies the conversion efficiency to $a(\lambda_p, \lambda_i, n + 1)$ with

$$\Delta a = a(\lambda_p, \lambda_i, n + 1) - a(\lambda_p, \lambda_i, n) \qquad (7)$$

and then

$$\begin{aligned}
I(\lambda_i, \lambda_p, n + 1) &= a(\lambda_p, \lambda_i, n + 1) I(\lambda_p, n + 1) \\
&= [a(\lambda_p, \lambda_i, n) + \Delta a][I(\lambda_p, n) + \Delta I_{\lambda_p})] \\
&= a(\lambda_p, \lambda_i, n) I(\lambda_p, n) + a(\lambda_p, \lambda_i, n) \Delta I_{\lambda_p} \\
&\quad + \Delta a I(\lambda_p, n) + \Delta a \Delta I_{\lambda_p}.
\end{aligned} \qquad (8)$$

We assume here the pump fluctuations to be small compared to the mean spectral intensity and the subsequent variation in the conversion efficiency to be small
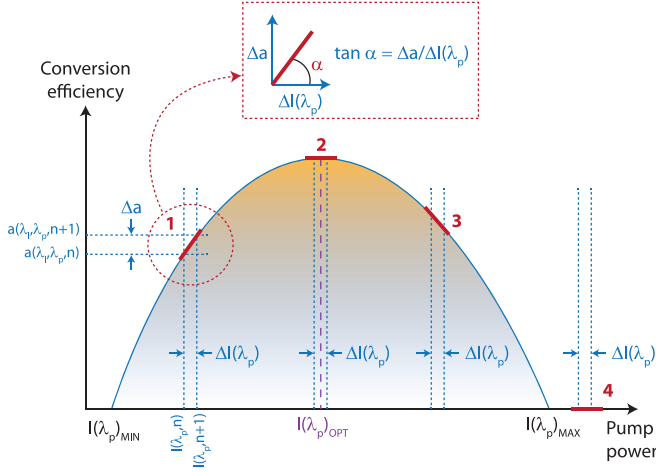
FIG. 3. Illustration of the effect of small changes in pump power at a specific wavelength on the conversion efficiency. The slope, denoted α and represented in red, can be null either at maximum conversion efficiency (2) or without any conversion at all (4).

compared to its mean value as well. We can therefore write

$$I(\lambda_i, \lambda_p, n+1) \approx a(\lambda_p, \lambda_i, n)I(\lambda_p, n)$$
$$+ a(\lambda_p, \lambda_i, n)\Delta I_{\lambda_p} + \Delta a I(\lambda_p, n) \quad (9)$$

$$\approx a(\lambda_p, \lambda_i, n)I(\lambda_p, n+1) + \Delta a I(\lambda_p, n), \quad (10)$$

and

$$\Delta I_{\lambda_i} \approx a(\lambda_p, \lambda_i, n)\Delta I_{\lambda_p} + \Delta a I(\lambda_p, n), \quad (11)$$

$$\Delta I_{\lambda_i}/\Delta I_{\lambda_p} \approx a(\lambda_p, \lambda_i, n) + (\Delta a/\Delta I_{\lambda_p})I(\lambda_p, n). \quad (12)$$

From a statistical point of view, we can then use a linear regression between λ_p and λ_i in order to isolate the effect of the pump on the idler, which is represented by $I(\lambda_i, \lambda_p, n)$ so that

$$I(\lambda_i, \lambda_p, n) = AI(\lambda_p, n) + B, \quad (13)$$

with the coefficients A and B being estimated by means of a regression between pump at wavelength λ_p and idler at wavelength λ_i,

$$\Delta I_{\lambda_i}/\Delta I_{\lambda_p} = A, \quad (14)$$

and as a result,

$$A = a(\lambda_p, \lambda_i, n) + (\Delta a/\Delta I_{\lambda_p})I(\lambda_p, n). \quad (15)$$

By using the standard LSQ method to obtain the best fit with the minimal error for a first-order polynomial, we can then estimate $\Delta I_{\lambda_i}/\Delta I_{\lambda_p}$, which represents the change in the idler due to the fluctuations in the spectral intensity of the pump at wavelength λ_p, as shown in Fig. 3. It then directly relates to the stability of the system. As a result, the derivative of the linear fit between the idler at wavelength λ_i and the pump at wavelength λ_p has a physical significance as it relates to the change of the conversion efficiency. It then directly quantifies the phase mismatch in addition to identifying the nature of the dependency between the two

wavelengths. In the following we then use this approach to plot comprehensive maps combining mutual information analysis and least-squares regression in order to study the full spectral dependency throughout the FOPO spectrum, both in the steady-state and build-up regimes. The combination between MI and linear regression is done by calculating the coefficient of proportionality A using a regression, while MI determines its trust level and acts as a validation mask. We then obtain a map displaying only the coefficient A, where the dependency between wavelengths is significant. Similarly to standard Pearson correlation maps [13], those maps actually allow for understanding and characterizing of the parametric gain distribution and will be referred to as MI-LSQ maps in the following.

IV. RESULTS AND DISCUSSION

A. Steady-state dynamics

1. Influence of small-intensity spectral fluctuations

The FOPO is pumped at a wavelength of 1563.5 nm with pulses featuring 28.5-ps duration, 3.12-nm spectral bandwidth, and 50-mW average power. The spectra of $\sim$2000 consecutive pulses were recorded, which corresponds to a temporal window of approximately 328 μs. The coefficient A in the resulting MI-LSQ map between idler and pump waves shown in Fig. 4(a) is estimated as an average over the whole time frame. We observe a set of thin vertical stripes in the spectral regions where the two peaks of the M-shaped pump spectrum are localized, from 1561.5 to 1563 nm and from 1565.5 to 1566.5 nm, respectively, as detailed in Fig. 4(c). These patterns extend throughout the whole idler spectrum, from 1646.7 to 1649.7 nm, which means that each pump component contributes to several or all idler wavelengths, each with a specific proportion as dictated by the phase-matching conditions. The vertical stripes switch their values between positive (red) and negative (blue), showing that the spectral fluctuations of the pump at a specific wavelength in the region of the peaks of the M-shaped spectrum have different effects on the conversion efficiency for each spectral component of the idler. These stripes also switch values with respect to the horizontal axis, indicating that the fluctuations on the different spectral components of the pump affect the conversion efficiency differently for a specific idler wavelength: a pump increase reduces the phase mismatch for certain wavelengths while it increases it for others. In addition, as the phase-matching conditions are different for the idler spectral components, this implies that the best possible conversion efficiency is achieved through the optimal compromise in the phase mismatch. We can also see in Fig. 4(b) that the vertical stripes change sign at around 1647.7-nm wavelength, which corresponds to the peak center of the idler. As previously illustrated in Fig. 3, the derivative of the conversion efficiency has indeed a minimal absolute value near its maximum (or when the conversion is nonexistent). This indicates that the pump spectral fluctuations have minimal effects on the conversion efficiency at the idler peak wavelength and that the conversion efficiency for this wavelength is maximal. We now consider the MI-LSQ map between signal and idler shown in Fig. 5. Based on energy conservation in DFWM in the specific case
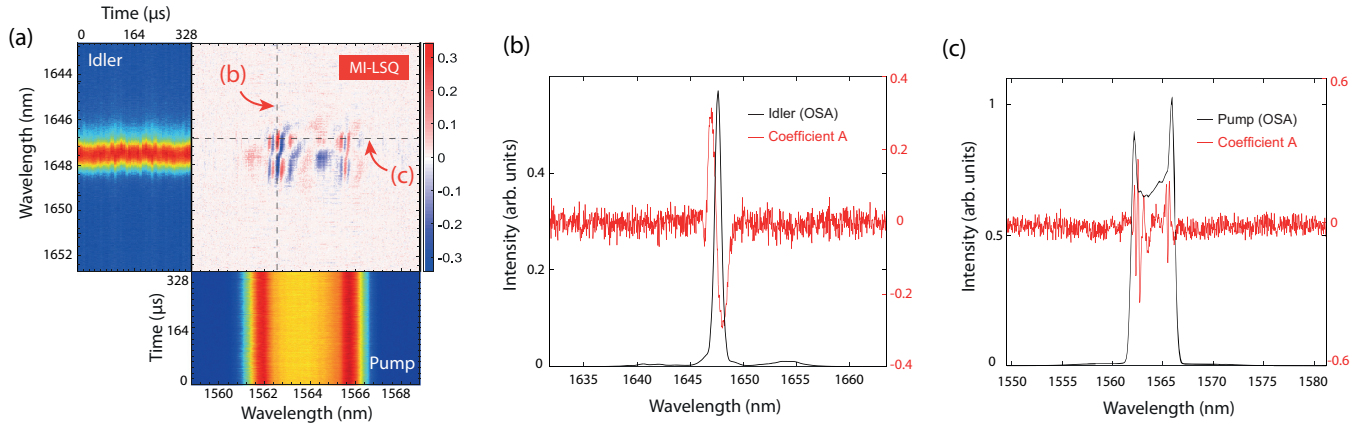
FIG. 4. (a) MI-LSQ map recorded on ~2000 consecutive shot-to-shot spectra between pump and idler waves. The color bar denotes the coefficient of proportionality A (red: proportional, blue: antiproportional). (b, c) Extraction of line profiles from the dotted lines on (a).

of chirped pump pulses (see, e.g., Ref. [13]), an idler-signal pair at frequencies ω_i and ω_s, respectively, can be generated only through the annihilation of two pump photons at a specific frequency ω_p where $\omega_i + \omega_s = 2\omega_p$. If we consider ω_s to be increasing linearly with respect to the dummy variable x,

$$\omega_s(x) = \omega_{s_0} + \frac{\partial \omega_s}{\partial x} x, \qquad (16)$$

with ω_{s_0} the lowest signal frequency component corresponding to:

$$\omega_{s_0} = \frac{2\pi c}{\lambda_{s_0} + \Lambda_{s_0}/2}. \qquad (17)$$

The energy conservation condition still holds for w_p only if

$$\omega_i(x) = \omega_{i_0} - \frac{\partial \omega_s}{\partial x} x \qquad (18)$$

with

$$\omega_{i_0} = \frac{2\pi c}{\lambda_{i_0} - \Lambda_{i_0}/2}. \qquad (19)$$

This leads to

$$\frac{\omega_i - \omega_{i_0}}{\omega_s - \omega_{s_0}} = -1. \qquad (20)$$

This indicates that if a change in the pump at frequency ω_p induced a change in the whole signal and idler spectra, the MI-LSQ map would exhibit a "proportionality" line with an inclination of $-45°$. Also, if the same thing occurs due to intensity fluctuations at a different pump frequency, it would result in a parallel line to the one we already have from pump at frequency ω_p [13]. In terms of wavelength, λ_i can then be written as a function of λ_p and λ_s as

$$\lambda_i = \frac{\lambda_p^2}{2(2\lambda_s - \lambda_p)} + \frac{\lambda_p}{2}. \qquad (21)$$

For a fixed λ_p, plotting λ_i as a function of λ_s then produces a quasilinear curve with an inclination of $-50.6°$, which does not intersect with curves generated from different pump wavelengths. This explains the localized red pattern on the diagonal of the map from which the pump spectral region responsible for the creation of the idler and signal pairs can be extracted (see Fig. 5). This region spans from ~1563 to ~1565 nm, corresponding to the wavelengths between the two peaks of the M-shaped spectrum. On the other hand, the blue patterns representing negative values on the signal or idler map are merely the effect of the modulation of the gain window of the signal and idler due to the pump intensity fluctuations, and it cannot be otherwise since the existence of an idler photon is conditional for the existence of a signal photon and vice versa.

We have then been able to visualize the effect of pump fluctuations on the conversion efficiency on a single wavelength basis as our method allowed for the generation of spectral maps with specific patterns directly related to the conversion efficiency. MI-LSQ maps thereby proved insightful regarding the system performance, as they allow one to track the energy flow from pump waves toward parametric waves.
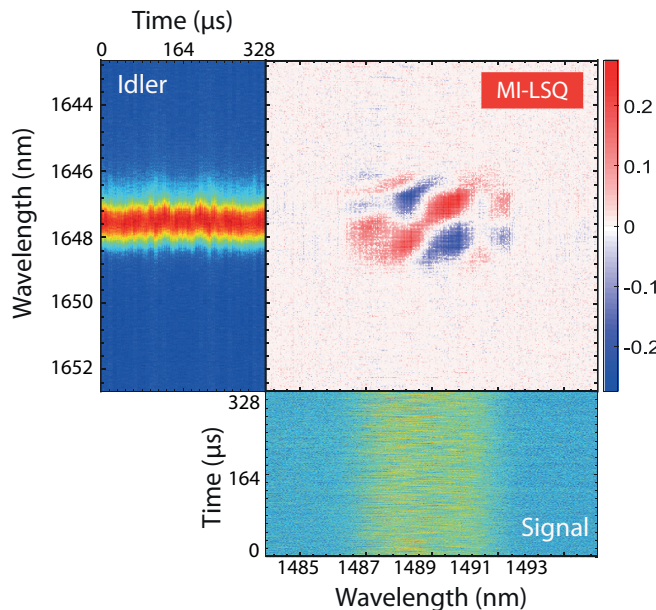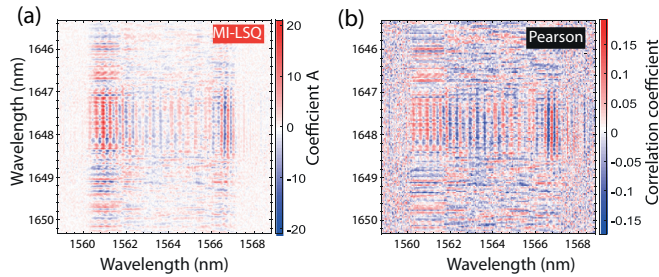

FIG. 5. MI-LSQ map between idler and signal waves.

FIG. 6. Pump vs idler MI-LSQ and standard Pearson correlation maps for a pump exhibiting large spectral intensity fluctuations: (a) MI-LSQ map and (b) standard Pearson correlation map.

2. Influence of large-intensity spectral fluctuations

In order to further investigate the effect of pump fluctuations on the conversion efficiency, the intensity level of the pump laser fluctuations was increased by inducing mechanical vibrations on the laser breadboard. Based on the DFT measurements, the mean spectrum of the pump did not change, but its mean standard deviation increased by 4.3%. The pump wave instabilities then led the idler and signal to exhibit considerable fluctuations: the conversion efficiency now oscillates between a high level with a strong pump depletion accompanied by a growth of signal and idler waves and a low level with a weakly depleted pump (see states 1 and 2 in Appendix A). The corresponding MI-LSQ map (pump vs idler) in Fig. 6(a) presents the same pattern compared to the stable pump case shown in the previous section, in contrast with the correlation map obtained using the standard Pearson correlation in Fig. 6(b), which exhibits a very poor contrast. MI-LSQ maps then prove superior to standard Pearson correlation maps for highlighting such fluctuations. In Fig. 6(a), we can still see localized modulations near the two peaks of the pump spectrum, while the value of coefficient A is much smaller in the central region. Strikingly, the value of coefficient A has increased by a factor of ~ 66 from a maximal absolute value of 0.3 [Fig. 4(a)] to 20, indicating that the idler's pump-induced fluctuations are up to 20 times greater than those of the pump itself. Figure 6 also shows that the two side peaks of the pump spectrum are mostly responsible for the violent idler and signal fluctuations. The idler and signal waves would then exhibit much weaker fluctuations and thereby be more immune to pump-induced noises if these peaks were somehow filtered out, as they have a negligible contribution to the DFWM process (see Appendix B). The change of conversion efficiency with respect to the pump power depicted in Fig. 3 explains this behavior, as the increase of the pump fluctuations in the spectral range where the conversion is maximal does not have a substantial effect on the conversion efficiency and does not cause fluctuations in the generated idler and signal (region 2 in Fig. 3). On the contrary, in regions 1 and 3, the greater the pump fluctuations, the greater the idler and signal fluctuations. In fact, if the pump intensity fluctuations exceed a given level, their effect on the idler and signal is amplified. This shows that the FOPO can tolerate pump instabilities (i.e., parametric wave fluctuations would be much smaller than the pump ones) until a certain limit where the signal and idler fluctuations would become much stronger and give rise to particular dy-
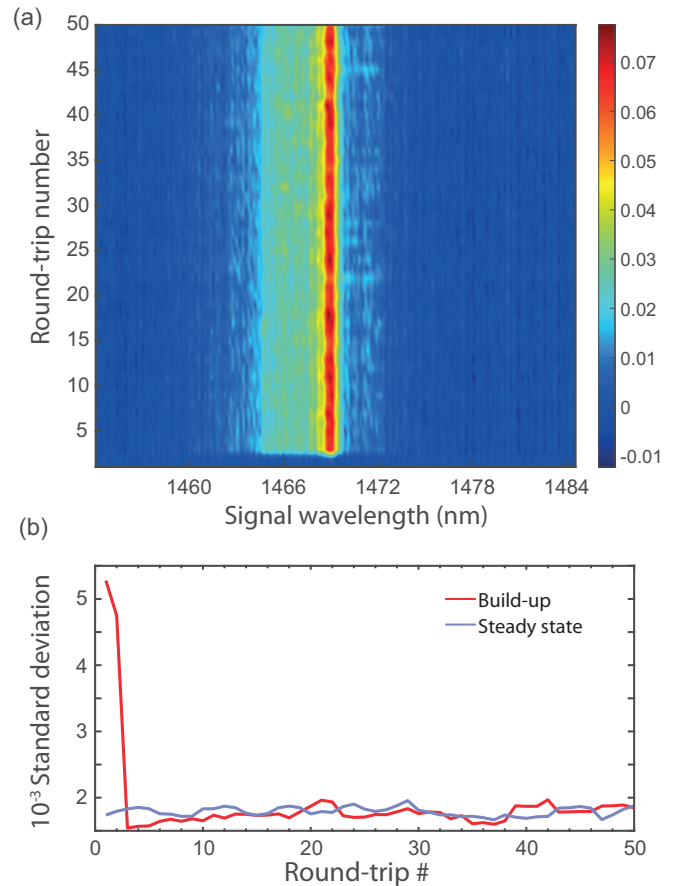

FIG. 7. (a) Pulse-to-pulse evolution of the FOPO's buildup. Only the first 50 shots are displayed, over a total of 10^5. (b) Moving standard deviation of the signal wave intensity in the build-up and steady-state regimes.

namics such as the two-states evolution mentioned previously. MI-LSQ maps then remarkably highlighted this phenomenon.

B. Spectrotemporal evolution and build-up regime

We studied the FOPO build-up dynamics by inserting an acousto-optic modulator (AOM, Fiber-Q, G&H Inc.) prior to the FOPO cavity, then allowing synchronization in time of the arrival of the first pump pulse with DFT measurements. In order to operate the AOM under optimal conditions, the pump laser is tuned to a central wavelength of 1560 nm. Using a mechanical chopper to modulate the pump beam and a 50/50 coupling ratio, a comparable study has recently shown that the steady state is reached after approximately 2000 round trips [25]. Here we differentiate from this study, as we use a much faster modulation—the AOM has a rise time of 35 ns—in order to prevent any extra transient dynamics. In addition, an appropriate coupling is also set to quickly reach stability. This latter parameter has indeed a considerable influence on the build-up dynamics as shown in Ref. [33]. Contrary to Ref. [25], we then observe that a signal wave is almost instantaneously generated, as shown in Fig. 7(a), where the steady state seems to be reached in the second round trip. For the sake of clarity, only 50 consecutive shots are displayed but a total of 10^5 spectra have actually been recorded. This result is also
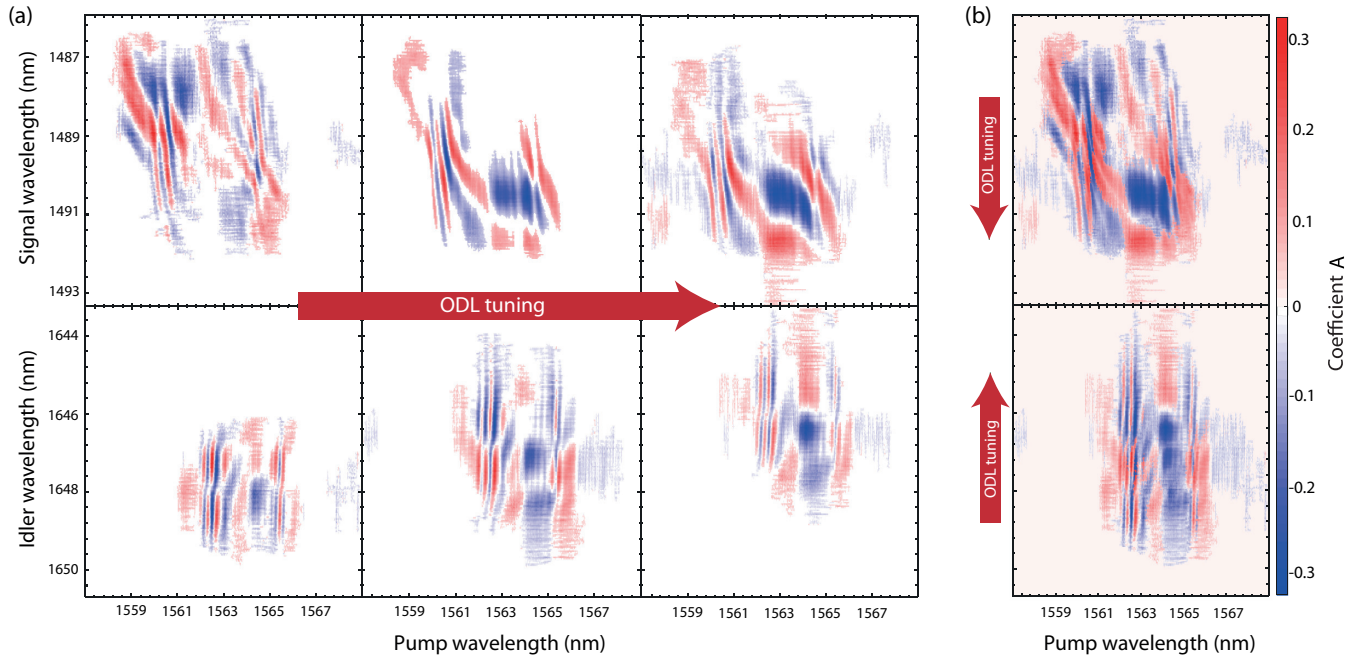
FIG. 8. MI-LSQ maps between pump and signal waves (top) and pump and idler (bottom) waves. (a) Maps recorded while varying the length of the optical delay line (ODL): initial length (left), ODL shortened by 50 μm (center), ODL shortened by 100 μm (right). (b) Synthesised maps superimposing the maps with different ODL lengths.

more consistent with previous numerical studies that indeed demonstrated that idler and signal waves were stabilized after only a few round trips [22,27,34]. In order to further prove that the steady state is reached, we computed the moving standard deviation over the recorded data and compared it with the steady-state case, as shown in Fig. 7(b). Here, the moving window contained four pulses. We then see that after a few round trips (less than 10), the standard deviation remains relatively stable with values similar to those in a well-established steady state. In both cases, small-scale fluctuations are attributed to the effect of pump-induced instabilities on the conversion efficiency.

C. Influence of time-dispersion tuning

In this last section, the mirror in the free-space part of the optical delay line (ODL) is displaced in order to change the phase-matching conditions and therefore to tune the idler and signal central wavelengths. Dispersion (GVD) in the passive fiber indeed stretches the resonating signal and idler, while the ODL length defines which portion of it is temporally synchronized with fresh pump pulses. Such a tuning of the FOPO output wavelengths is referred to as time-dispersion tuning [27] and allows a broad tunability. We then recorded the MI-LSQ maps between idler and pump waves while tuning the ODL, as shown in Fig. 8(a).

These figures show that the further we reduce the length of the ODL, the higher the coefficient A in the spectral region between 1562.5 and 1565 nm with respect to the horizontal axis. The increase of the proportionality coefficient implies a reduction in the conversion efficiency, which is consistent with the attenuation of the idler's peak. On the other hand, we can also see in Fig. 8(b) that the map between pump and signal

waves based on their corresponding maps at different ODL lengths shows a continuous pattern that displaces vertically while tuning. As the coefficients on these maps relate physically to the conversion efficiency in the present conditions of the system, changes in ODL dispersion and length thereby allow for a certain shaping of the MI-LSQ maps by selecting vertically the width and center of the region of the map to appear. Such a technique could then now be optimized for selecting the correlated wavelengths of interest and then prove useful in the framework of tailoring correlations for specific applications.

V. CONCLUSION

In summary, we used an original combination of statistical tools to investigate the dynamics of a normal dispersion picosecond fiber-optical parametric oscillator (FOPO) using time-stretch spectroscopy. This method not only allows one to track the energy transfer from pump to signal/idler pairs, but also visually quantifies the state of this energy conversion on a single wavelength basis. The outcomes of this study are then manifolds: (i) the combination of mutual information (MI) analysis with least-squares (LSQ) regression is very efficient to extract relevant information on the dynamics of the system and proves superior to standard Pearson correlations for revealing its specific dynamics, (ii) the increase of pump intensity fluctuations above a certain level results in particular unstable output dynamics, as pump fluctuations can be amplified up to 20 times when converted to the idler wave, (iii) the FOPO reaches the steady state in the first few round trips, and (iv) the spectral correlations can be shaped to a certain extent by varying the phase-matching conditions of the oscillator, a feature that could prove useful for specific quantum optics
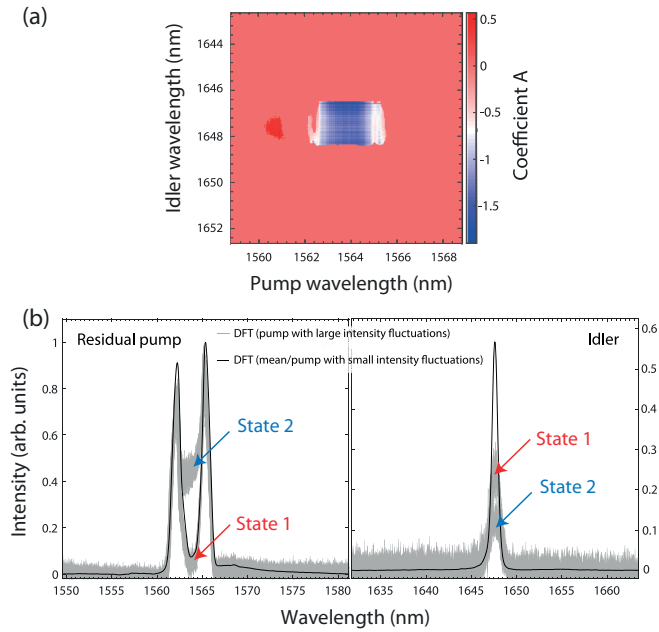
FIG. 9. (a) Pump vs idler MI-LSQ map recorded on ∼2000 consecutive shot-to-shot spectra with a fluctuating pump. (b) Consecutive spectra for the residual pump and idler components compared with the spectra obtained with a stabler pump.

FIG. 10. Average pump and residual pump spectra (bottom) and calculated relative pump depletion (top).

applications. We then believe that this approach combining MI and LSQ could now be routinely used to explore specific spectrotemporal dynamics and also that these kinds of measurements could be complementary to other tools such as temporal statistics [35] to further comprehend and control the intrinsic dynamics of ultrafast optical systems.

APPENDIX A: EFFECT OF SIGNIFICANT PUMP FLUCTUATIONS ON THE CONVERSION EFFICIENCY

Here we show the effect of large pump intensity fluctuations on the conversion efficiency through the recording of
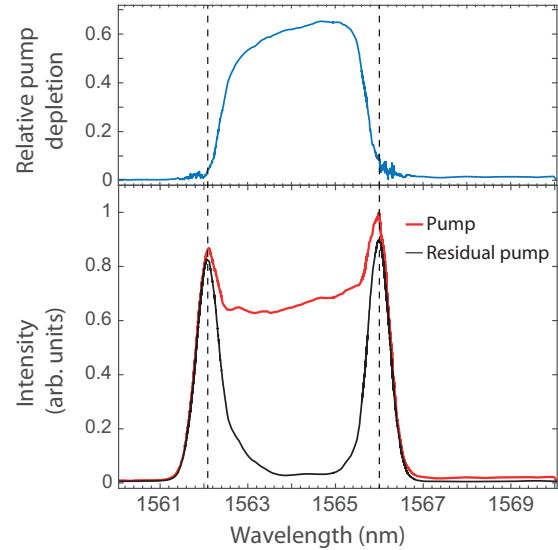
shot-to-shot spectra of the residual pump and idler along with generating their respective MI-LSQ map. The consecutive spectra for the residual pump and idler, shown in Fig. 9(b), evidence that their spectral intensities exhibit very large fluctuations. In this case the conversion efficiency oscillates between a high level with a strong pump depletion accompanied by a growth of signal and idler waves (state 2) and a low level with a mostly undepleted pump (state 1). An inverse proportionality relationship between the residual pump and idler can easily be deduced from the MI-LSQ map in Fig. 9(a) as the coefficient of proportionality A is purely negative (blue region).

APPENDIX B: PUMP DEPLETION VERSUS WAVELENGTH

In order to clearly highlight that the central part of the pump spectrum contributes the most to the DFWM process and that the side peaks have negligible influence, Fig. 10 represents the relative pump depletion as a function of wavelength and compares average normalized pump and depleted pump spectra. It then clearly appears that the depletion is much stronger the central region of the M-shaped spectrum, where the relative pump depletion exceeds 50% for most of the wavelengths while it is below 10% in the side peaks (vertical dotted lines). This proves this central spectral region to be predominantly contributing to DFWM.

[1] A. Tikan, S. Bielawski, C. Szwaj, S. Randoux, and P. Suret, Nat. Photon. **12**, 228 (2018).

[2] P. Ryczkowski, M. Närhi, C. Billet, J.-M. Merolla, G. Genty, and J. M. Dudley, Nat. Photon. **12**, 221 (2018).

[3] A. Mahjoubfar, D. V. Churkin, S. Barland, N. Broderick, S. K. Turitsyn, and B. Jalali, Nat. Photon. **11**, 341 (2017).

[4] K. Goda and B. Jalali, Nat. Photon. **7**, 102 (2013).

[5] G. Herink, B. Jalali, C. Ropers, and D. R. Solli, Nat. Photon. **10**, 321 (2016).

[6] G. Herink, F. Kurtz, B. Jalali, D. R. Solli, and C. Ropers, Science **356**, 50 (2017).

[7] K. Krupa, K. Nithyanandan, U. Andral, P. Tchofo-Dinda, and P. Grelu, Phys. Rev. Lett. **118**, 243901 (2017).

[8] B. Wetzel, A. Stefani, L. Larger, P. A. Lacourt, J. M. Merolla, T. Sylvestre, A. Kudlinski, A. Mussot, G. Genty, F. Dias *et al.*, Sci. Rep. **2**, 882 (2012).

[9] T. Godin, B. Wetzel, T. Sylvestre, L. Larger, A. Kudlinski, A. Mussot, A. B. Salem, M. Zghal, G. Genty, F. Dias *et al.*, Opt. Express **21**, 18452 (2013).

[10] D. R. Solli, G. Herink, B. Jalali, and C. Ropers, Nat. Photon. **6**, 463 (2012).

[11] X. Wang, D. Bigourd, A. Kudlinski, K. K. Y. Wong, M. Douay, L. Bigot, A. Lerouge, Y. Quiquempois, and A. Mussot, Opt. Lett. **39**, 1881 (2014).

[12] S. Sugavanam, M. Sorokina, and D. V. Churkin, Nat. Commun. **8**, 15514 (2017).

[13] P. Robert, C. Fourcade-Dutin, R. Dauliat, R. Jamier, H. Muñoz-Marco, P. Pérez-Millán, J. M. Dudley, P. Roy, H. Maillotte, and D. Bigourd, Opt. Lett. **45**, 4148 (2020).

[14] M. Barbier, I. Zaquine, and P. Delaye, New J. Phys. **17**, 053031 (2015).

[15] M. A. Finger, N. Y. Joly, P. S. J. Russell, and M. V. Chekhova, Phys. Rev. A **95**, 053814 (2017).

[16] M. Cordier, A. Orieux, B. Debord, F. Gérome, A. Gorse, M. Chafer, E. Diamanti, P. Delaye, F. Benabid, and I. Zaquine, Opt. Express **27**, 9803 (2019).

[17] J. Roslund, R. M. de Araújo, S. Jiang, C. Fabre, and N. Treps, Nat. Photon. **8**, 109 (2014).

[18] J. Laurat, L. Longchambon, C. Fabre, and T. Coudreau, Opt. Lett. **30**, 1177 (2005).

[19] D. Descloux, C. Laporte, J.-B. Dherbecourt, J.-M. Melkonian, M. Raybaut, C. Drag, and A. Godard, Opt. Lett. **40**, 280 (2015).

[20] K. Ivanauskienė, I. Stasevičius, M. Vengris, and V. Sirutkaitis, J. Opt. Soc. Am. B **36**, 131 (2019).

[21] G.-L. Oppo, A. M. Yao, and D. Cuozzo, Phys. Rev. A **88**, 043813 (2013).

[22] T. Gottschall, T. Meyer, M. Schmitt, J. Popp, J. Limpert, and A. Tünnermann, Opt. Express **23**, 23968 (2015).

[23] C. Xu and F. W. Wise, Nat. Photon. **7**, 875 (2013).

[24] E. S. Lamb, S. Lefrancois, M. Ji, W. J. Wadsworth, X. S. Xie, and F. W. Wise, Opt. Lett. **38**, 4154 (2013).

[25] X. Chen, S. Yang, S. Ding, M. Chen, and H. Chen, IEEE Photon. Technol. Lett. **31**, 1088 (2019).

[26] M. C. Soriano, L. Zunino, O. A. Rosso, I. Fischer, and C. R. Mirasso, IEEE J. Quantum Electron. **47**, 252 (2011).

[27] R. Becheker, M. Tang, P.-H. Hanzard, A. Tyazhev, A. Mussot, A. Kudlinski, A. Kellou, J.-L. Oudar, T. Godin, and A. Hideur, J. Phys. Lett. **15**, 115103 (2018).

[28] M. Tang, H. Wang, R. Becheker, J.-L. Oudar, D. Gaponov, T. Godin, and A. Hideur, Opt. Lett. **40**, 1414 (2015).

[29] T. M. Cover and J. A. Thomas, *Elements of Information Theory* (Wiley, New York, 2006).

[30] J. Peng, M. Sorokina, S. Sugavanam, N. Tarasov, D. V. Churkin, S. K. Turitsyn, and H. Zeng, Commun. Phys. **1**, 20 (2018).

[31] J. Seok and Y. Seon Kang, Sci. Rep. **5**, 2045 (2015).

[32] T. Sylvestre, H. Maillotte, E. Lantz, and F. Devaux, Opt. Commun. **191**, 245 (2001).

[33] M. Brinkmann, T. Hellwig, and C. Fallnich, Opt. Express **25**, 12884 (2017).

[34] T. Gottschall, J. Limpert, and A. Tünnermann, Opt. Lett. **42**, 3423 (2017).

[35] K. Nagashima, Y. Ochi, and R. Itakura, J. Opt. Soc. Am. B **36**, 3389 (2019).